

# Paper NA

Pierre

April 27, 2017

## 1 Introduction

The North American continent consists of an ancient cratonic core, formed during the Archean, that has not been subjected to orogeny for at least 1.8 Ga, bordered to the southeast and east, by progressively younger, stable, Proterozoic provinces (Hoffman 1988). In the west, the Rocky Mountain Front (RMF) separates the Proterozoic and Archean shield from younger, tectonically active provinces (Fig. 1). This relatively regular configuration makes North America an ideal target for seismic tomography, to investigate the relationship of lithospheric and asthenospheric structure to the geological features observed at the surface.

Differences in the seismic velocity structure between the craton and the western US extending down to at least 200 km were established already in the 1960's and 70's from the first studies of teleseismic P and S wave travel time anomalies (e.g. Cleary and Hales 1966, Herrin and Taggart 1968, Poupinet 1979), the first tomographic images based on P and S travel times (Romanowicz 1979) and long period surface waveforms (Woodhouse and Dziewonski 1984), as well as contrasted velocity-depth profiles obtained from the modeling of shear body waveforms at relatively short distances (e.g. Grand and Helmberger 1984). More recent body wave tomographic models have added considerable details to these images (Sigloch 2011, Burdick et al. 2014, Porritt et al. 2014; 2015)

Lateral variations in absolute velocities can be inferred from shear wave tomography, at scales from global (e.g. Su et al. 1994, Mégnin and Romanowicz 2000, Shapiro and Ritzwoller 2002, Panning and Romanowicz 2006, Kuszowski et al. 2008, Ritsema et al. 2010, Lekić and Romanowicz 2011, Debayle and Ricard 2012, Schaeffer and Lebedev 2013) to continental (van der Lee and Frederiksen 2005, Yuan et al. 2011; 2014, Schaeffer and Lebedev 2014). These studies confirm the presence of strong lateral variations in the thickness of the lithosphere across the RMF, with lithospheric roots extending

down to 200-250 km under the craton, thinning abruptly to the west to less than 80-100 km. This is also found from azimuthal anisotropy tomography, where a change in the anisotropy fast axis direction across the lithosphere-asthenosphere boundary (LAB) ([Marone and Romanowicz 2007](#), [Yuan and Romanowicz 2010](#)).

While the mechanism of craton formation is still widely debated (e.g. [King 2005](#), [Lee et al. 2011](#)), the presence of finer scale lateral and depth variations ([cite some body wave tomography studies](#) in seismic structure suggest a complex history. Moreover, studies of azimuthal anisotropy have shown the presence of laterally varying layering within the cratonic lithosphere (e.g. [Levin et al. 1999](#), [Deschamps et al. 2008](#), [Yuan and Romanowicz 2010](#)), which may indicate different modes and/or times of formation of the top c.a. 100 km of this lithosphere. Fine scale studies of converted and reflected phases indicate the presence of a sharp mid-lithospheric discontinuity (MLD) within the craton, marking the top of a mid-lithospheric low velocity zone ([Thybo and Perchu 1997](#), [Bostock 1998](#), [Abt et al. 2010](#), [Fischer et al. 2010](#), [Rader et al. 2015](#), [Ford et al. 2016](#)) and even possibly several mid-lithospheric discontinuities ([Calò et al. 2016](#)). In addition, there is evidence from radially anisotropic shear wave tomography for separation between blocks of different

crustal ages extending to depths of at least 150 km (e.g. Yuan et al. 2014).

Much of this finer scale structure has been resolved owing to the availability of data from the dense broadband USArray TA deployment. With the completion of the coverage of the conterminous US, as well as availability of data from Canada and Greenland, it is now possible to further refine shear wave tomographic images of North America, and in particular of the stable Proterozoic and Archean provinces, to try and improve our understanding of the different stages of formation of the continent. It is also an unprecedented opportunity to experiment with improved waveform-based tomographic techniques.

In a previous study, we presented a radially anisotropic shear velocity model of the North American upper mantle based on a combination of long period teleseismic and regional waveform data (Yuan et al. 2014). The regional waveform data (down to 40 s period) were, for the first time at this scale, compared to 3D synthetics computed using RegSEM (Cupillard et al. 2012), a Spectral Element Method (SEM) code suitable for continental-scale wavefield computations. Due to the very heavy computations that would have been necessary to compute the predicted teleseismic wavefield numerically at each iteration of the inversion, the latter was, instead, computed

using Non-Linear Assymptotic Coupling Theory (NACT, [Li and Romanowicz 1995](#)), a methodology based on normal mode perturbation theory, that is computationally more efficient (albeit approximate), and has been used in the development of several generations of global and continental scale shear velocity models based on time-domain waveform inversion ([Li and Romanowicz 1996](#), [Mégnin and Romanowicz 2000](#), [Gung et al. 2003](#), [Panning and Romanowicz 2006](#), [Yuan et al. 2011](#))

The resulting 2014 model of North America presents some interesting features, in particular a correlation of radial anisotropy structure with lithospheric blocks corresponding to different orogenies in the eastern US and continental shelf. While more rigorous than inversions practiced by most groups and based on the path-average surface wave approximation (PAVA, [Woodhouse and Dziewonski 1984](#)), this mixed methodology nevertheless presents some inconsistencies from the theoretical point of view, since the predicted wavefield through the target model space is computed with different theories for teleseismic and regional distance data, respectively.

To better integrate teleseismic data into our regional tomographic inversions, we developed a general framework called "Box Tomography" (see [Masson et al. 2013](#), [Masson and Romanowicz 2016; 2017](#)), that allow us to

consistently model and invert both teleseismic (i.e. associated with sources or receivers outside of the imaged region) and regional (i.e. associated with sources and receivers within the imaged region) waveform data using accurate numerical methods such as SEM. In Box Tomography, prior to the inversion, the seismic wavefield generated by teleseismic sources is first modeled numerically at the global scale for a given reference 3D model and is recorded at the surface of the region to be imaged. This reference wavefield is then used to construct virtual sources lying at the boundary of the regional modeling domain and reproducing the original wavefield as illustrated in Figure 4. Once the teleseismic sources have been moved (i.e. replaced by virtual sources) within the regional modeling domain, the tomographic inversion can be performed efficiently in a classical manner (i.e. using regional modeling only) as the teleseismic data are accounted for seamlessly thanks to the virtual sources. Related concepts have been proposed to account for teleseismic data in regional imaging (e.g. Wang et al., 2016 Monteiller et al., 2015), however, in these studies the global modeling of the reference wavefield is performed using a faster method that does not account for the effects induced by the 3D structure of the Earth outside the regional modeling domain. In this paper, we present the first application of Box Tomography to

continental scale waveform tomography in North America.

## 2 Methodology

Many studies have inverted for continental scale structure, in particular in North America, using fundamental mode and, in some cases, overtone surface wave dispersion data or waveforms observed at teleseismic distances. The usual practice is to first consider the best possible global scale tomographic shear wave velocity model, compute predictions of observables in this model using an approximate theory, generally the surface wave path average approximation (e.g. Nettles and Dziewoński 2008, Bedle and van der Lee 2009, Schaeffer and Lebedev 2014), or, in our group, NACT (Marone et al. 2007, Yuan et al. 2011). In the case when secondary observables such as dispersion data are considered, the contribution from outside of the target region is calculated once and for all in the background global model, and subtracted from the observed dispersion data. The resulting residual is attributed to structure in the target region and the tomographic inversion proceeds within this target model volume. When inverting waveforms, and in particular when a more accurate theory than the PAVA is considered,

such a simple procedure is not possible, and it is necessary to recompute the synthetic teleseismic waveforms, at each iteration, in a 3D model which is fixed outside of the target region, and updated only within it. This leads to substantial computations, even in the case of an approximate theory such as NACT, and becomes prohibitively expensive, if the 3D teleseismic wavefield is computed using SEM or another accurate numerical method, as especially as one aims to include increasingly shorter periods.

To overcome this problem, we take advantage of the "Box Tomography" theory which allows us to combine teleseismic and regional waveforms in a consistent manner to image regional targets at arbitrary locations. This general framework accommodates for arbitrary acquisition setups (i.e. with sources and receivers located outside the regional imaging box), is compatible with most popular numerical methods such as SEM or FD, and can produce exact seismograms and sensitivity kernels (i.e. similar to those obtained when solving the problem globally). In this study, we limit ourselves to the situation where both regional and teleseismic events are employed but where all the seismic stations lie within the regional computational domain. Furthermore, we neglect some higher order scattering effects, as proposed by [Masson and Romanowicz \(2016\)](#). In this situation, Box Tomography is

particularly efficient, as the computational effort to account for teleseismic data in regional inversions is limited to a few global scale simulations that are done once and for all prior to the inversion. [Masson and Romanowicz \(2016\)](#) showed that this approach can produce accurate regional tomographic images even though the elastic structure outside the imaged region is neither fully known prior to the inversion, nor updated during the inversion.

Here, we apply this methodology to the case of teleseismic three component waveform data observed at stations within North America, combined with "regional" waveform data for which both earthquakes and stations are located within the target region. This is the first time this methodology is applied in practice, and this study represents a proof of concept for this approach. Adding teleseismic data allows better azimuthal coverage of the target region than can be achieved using only the regional dataset, and eventually provides for the inclusion of constraints from additional phases such as, for example, teleseismic SS phases reflected inside the target region.

## 2.1 Dataset and model parametrization

.

The dataset includes three component acceleration waveforms from 2860

permanent and temporary broadband stations located in the target region, a  $89^\circ \times 89^\circ$  area encompassing most of north America (Figure 2). We considered two different datasets:

- a regional dataset consisting of 155 events ( $4.5 < M_w < 6.0$ ) for which sources are located within the target region.
- a teleseismic dataset, consisting of 122 events ( $5.5 < M_w < 6.9$ ) for which sources are located outside of the target region.

The waveforms are filtered between 40 and 400 s, with corner frequencies at 53 and 250 s, and windowed into wavepackets, according to the procedure of Li and Romanowicz (1996), allowing different weights to be applied according to relative amplitude of individual wavepackets, redundancy of paths and signal to noise ratio. This weighting step is crucial, as it homogenizes the data coverage within the region and provides a way to construct the data covariance matrix  $C_D$ , which we approximate as a diagonal matrix. At each iteration of the inversion, only those wavepackets are considered that satisfy predefined goodness of fit criteria compared to synthetics calculated in the current 3D model, in particular to avoid cycle slipping in our time domain waveform inversion procedure. As the model improves, at each iteration,

additional wavepackets are included. The total number of wavepackets of fundamental and overtone Love and Rayleigh waves is given in Table 1, and provides a good coverage within the NA continent (Figure 3).

In addition to long period waveforms, we also consider a group velocity dispersion dataset (Shapiro and Ritzwoller 2002) provided in the form of  $1^\circ \times 1^\circ$  maps between 25 and 100 s. The shorter periods (below 60 s) are used to constrain our homogenized crustal structure at each iteration, as described below, while the entire period range is included during the inversion for mantle structure, providing additional constraints for structure in the shallow parts of the mantle, that are consistent with the treatment of the crust.

As in our previous work at the global scale (French et al. 2013, French and Romanowicz 2014), we do not rely on an existing layered crustal model. There are several drawbacks to considering such models. First, they are constructed using data for limited regions that are then extrapolated to other regions based on a tectonic regionalization, and may not always fit real waveform data very well. Second, the inclusion of thin low velocity layers slows down the SEM computation significantly. Instead, we compute a radially anisotropic smooth crustal model on a  $2^\circ \times 2^\circ$  grid through Monte Carlo

Markov Chain (MCMC) simulation constrained by the group velocity dispersion data.

This process is called "homogenization" (e.g. [Backus 1962](#), [Capdeville and Marigo 2008](#)), and yields a crustal model equivalent to a real crust within the period range of the data used to constrain it (i.e. here for periods longer than 20s). The thickness of the crust is a priori fixed to that of model Crust2.0 ([Bassin et al. 2000](#)) when it is larger or equal to 30 km, and it is fixed at 30 km in regions where it is thinner. This results in a smooth, but realistic crust within most of the continent, and a crustal model that is not directly interpretable in the border regions of our model space (i.e. in the oceans and borders of the continent where the real crust is thin). We have shown that this does not bias the mantle structure imaged below 50 km ([French and Romanowicz 2014](#)). At each iteration of the inversion, we only invert for structure below 30 km depth, and subsequently recompute the crustal model for the next iteration by applying our MCMC approach with mantle structure fixed to that of the current iteration model. The procedure is described and discussed in detail in [French and Romanowicz \(2014\)](#)

Assuming that our azimuthal coverage is everywhere sufficient within our target region, we here solve only for radially anisotropic structure. If

(A,C,F,L and N) are the 5 elastic parameters describing a radially anisotropic (or VTI) medium ([Love 2013](#)), then:

$$N = \rho V_{SH}^2, \quad L = \rho V_{SV}^2, \quad A = \rho V_{PH}^2, \quad C = \rho V_{PV}^2 \quad (1)$$

then the medium can equivalently be described by the 5 parameters  $(V_S, V_P, \xi, \phi, \varepsilon)$  where:

$$V_S = \sqrt{\frac{2V_{SV}^2 + V_{SH}^2}{3}} V_P = \sqrt{\frac{V_{PV}^2 + 4V_{PH}^2}{5}} \xi = \frac{N}{L}, \quad \varphi = \frac{C}{A}, \quad \eta = \frac{F}{A - 2L} \quad (2)$$

We only consider two of the 5 independent anisotropic parameters , those to which long period surface waveforms are the most sensitive: isotropic velocity  $V_S$  and the anisotropic parameter  $\xi = \frac{V_{SH}}{V_{SV}}^2$ , where  $V_{SH}$  is the velocity of waves polarized horizontally and  $V_{SV}$  that of waves polarized vertically . The other three parameters and density are constrained through empirical scaling relationships, following [Montagner and Anderson \(1989\)](#), and are based on laboratory measurements for upper mantle rocks.

The scaling parameters considered are ([Montagner and Anderson 1989](#))

$$\frac{\delta(V_P)}{\delta(V_S)} = 0.5, \quad \frac{\delta(\rho)}{\delta(V_S)} = 0.33, \quad \frac{\delta(\eta)}{\delta(\xi)} = -2.5, \quad \frac{\delta(\varphi)}{\delta(\xi)} = -1.5, \quad (3)$$

We chose a parametrization in terms of  $V_S$  and  $\xi$ , rather than  $V_{SH}$  and  $V_{SV}$ , as this allows us to consider different spatial resolution and apply higher damping in the inversion to the less well resolved anisotropic parameter  $\xi$ , rather than having to reconstruct this parameter from differences in perturbations in the two quantities  $V_{SH}$  and  $V_{SV}$ , which would limit the resolution allowed in isotropic velocity.

In previous studies ([Marone and Romanowicz 2007](#), [Yuan and Romanowicz 2010](#)), after inverting for radial anisotropic structure ([Marone et al. 2007](#), [Yuan et al. 2011](#)), we also inverted for azimuthal anisotropy, by adding constraints from SKS splitting measurements. This step will be the topic of a separate publication.

The target model space is geographically defined as shown in Figure 2, and is limited in depth down to 800 km. As in our previous tomographic studies, the model space is parametrized in terms of 26 cubic splines  $\nu_q(r)$  vertically ([Mégnin and Romanowicz 2000](#)) from the core-mantle boundary to 30 km deep. Although we invert for structure only in the top 16 splines, corresponding to the top 700-800 km of the mantle. The spline nodes are

spaced more closely at shallow depths, and located at the following radii: 5690, 5810, 5910, 5900, 6061, 6101, 6131, 6161, 6191, 6221, 6241, 6261, 6281, 6301, 6321, 6341 km. Laterally, we parametrize our model in terms of spherical splines  $\beta(\theta, \phi)_p$  (Wang and Dahlen 1995). The combination of vertical and spherical splines constitutes a local basis for the description of smooth functions within the model volume. Thus, the value of a model parameter  $m(r, \theta, \phi)$  can be computed at any point in space given the set of spline coefficients  $m_{pq}$ :

$$m(\theta, \varphi, r) = \sum_p \sum_q m_{pq} \beta_p(\theta, \varphi) \nu_q(r) \quad (4)$$

The spherical spline parametrization has the advantage of allowing for variable grid parametrization, which can be adjusted according to data coverage (e.g. Marone et al. 2007). In our case, outside of the target region, we adopt a "level 6" spherical grid for  $V_S$  ( $2^\circ$  knot spacing) and a "level 4" spherical grid for  $\xi$  ( $8^\circ$  knot spacing), consistent with the parametrization of *SEMUCB-wm1* (French and Romanowicz 2014). Inside the well-sampled target region, we define a level 7 spherical grid ( $1^\circ$  knot spacing) for  $V_S$  and level 6 ( $2^\circ$  knot spacing) for  $\xi$ .

## 2.2 Forward modelling

During the inversion, all the synthetic seismograms are computed using the regional SEM code RegSEM ([Cupillard et al. 2012](#)) that takes into account effects of oceans, topography/bathymetry, ellipticity, and anelasticity, and where the limits of the computational domain (white box around North America in Figure [4](#) and red box in Figure [2](#)) are dealt with using absorbing boundaries. The synthetic seismograms associated with regional data (i.e. where both the seismic stations and the earthquake are located within the regional modeling domain) do not require any specific treatment and are computed as in our previous studies using RegSEM (e.g. [Yuan et al. 2014](#)). The synthetic seismograms associated with teleseismic data (i.e. where the earthquake and the seismic stations are located outside and inside the regional modeling domain, respectively) are obtained using a two step procedure as proposed by [Masson and Romanowicz \(2016\)](#) as follows.

Prior to the inversion, the wavefields generated by teleseismic earthquakes are computed globally within our starting model (*SEMucb\_wm1*) and a version of *SPECFEM3D\_globe* ([Komatitsch 2002](#)) adapted to this model representation. During these global simulations, the 3 component displacement wavefield is recorded at a set of points with locations prescribed by

the RegSEM code. Within the regional solver RegSEM, these points are the collocation or Gauss-Lobatto-Legendre (GLL) points belonging to the one element thick surface surrounding the regional modeling domain (see Masson et al. 2013). Note that our procedure does not require to store either the stress or the strain wavefield, which are computed naturally by the regional solver. This makes it easy to swap between different codes for modeling global seismic wave propagation (i.e. any code that outputs displacement seismograms can be used as such). Because the Courant criteria which ensure the stability in SEM often lead to oversampling, we compress the recordings versus time using a least square B-spline transform (Unser et al. 1993a,b). We found this approach more efficient and practical than the more classic decimation/interpolation scheme. We typically achieve a data compression ratio of between 10 and 100 with no significant loss of accuracy. During the inversion, the global recordings are transformed to virtual sources that regenerate the global wavefield regionally. This operation is done on the fly by the RegSEM code.

Overall, the additional computational effort to account for teleseismic events consists of one global simulation per teleseismic event. These simulations are done once and for all before the inversion starts. A comparison

between regular *SPECFEM3D\_globe* and “RegSEM + virtual sources“ synthetics is shown in Figure 4.

## 2.3 Inverse modelling

In continuity of our previous work (e.g Marone et al. 2007, Yuan et al. 2011; 2014), we use a hybrid iterative inversion scheme where, at each iteration, the forward wavefield is computed accurately using SEM, but the inverse step is solved using the formalism of Tarantola and Valette (1982) with sensitivity kernels calculated approximately using normal mode perturbation theory. This allows us to apply a fast converging Gauss-Newton quadratic optimization scheme. As shown in Tarantola (2005), and in Appendix A of Lekić and Romanowicz (2011), it is far more important to use an accurate forward modelling scheme to compute the misfit function, provided of course that the theory captures the effects of the background long wavelength structure accurately (unlike the examples shown in Valentine and Trampert 2016). Inaccuracies in the theoretical treatment of kernels then result in smoothing errors that can be compensated for in subsequent iterations. In contrast, currently popular ”adjoint tomographic“ approaches (Zhu et al. 2015, Bozdağ et al. 2016) compute the numerically exact gradient, however, they also need

to apply smoothing operators and regularization, which degrades the accuracy of their kernels. Importantly, they rely on a linear optimization scheme (conjugate gradient method), which is characterized by very slow convergence.

Our misfit function is defined in the time domain from the point by point differences between observed and synthetic waveforms as follows:

$$2\Phi(m_k) = [d - g(m_k)]^T C_d^{-1} [d - g(m_k)] + [m_p - m_k]^T C_m^{-1} [m_p - m_k] \quad (5)$$

where  $m_k$  represents the model estimate at the k-th iteration,  $d$  is the data vector (waveform discretized in time or group velocity as a function of period) and  $g(m_k)$  is the corresponding discretized wavefield computed using SEM, or the predicted group velocity dispersion. The model prior is  $m_p$  (i.e. the 3D starting model) and  $C_m$  and  $C_d$  represent a priori model and data covariance matrices, respectively. Minimizing  $\Phi$  in the sense of the L2 norm leads to the equation for the k+1 model update:

$$m_{k+1} = m_k + (C_m G_k^T C_d^{-1} G_k + I)^{-1} (C_m G_k^T C_d^{-1} [d - g(m_k)] + m_p - m_k) \quad (6)$$

where  $G$  is the matrix of Frechet derivatives of  $g(m)$  calculated at  $m_k$ . We compute  $G$  using NACT or PAVA, depending on the distance range of the cor-

responding source-station path. NACT and PAVA are both asymptotic (high frequency) approximations to first order normal mode perturbation theory. The PAVA includes along branch mode coupling only and is equivalent to the standard surface wave approximation (e.g [Mochizuki 1986](#), [Romanowicz 1987](#)), as used for example in [Woodhouse and Dziewonski \(1984\)](#), in which a frequency shift and distance shift are introduced for each mode to account for the effects of heterogeneous structure. The corresponding kernels are "1D", i.e. they only depend on the average structure between the source and the receiver. This approximation is valid for single-mode seismograms, such as fundamental mode surface waves (e.g [Romanowicz et al. 2008](#)). NACT includes across branch-coupling, in addition to PAVA, which brings out 2D sensitivity of waveforms in the vertical plane containing the source and the receiver. NACT breaks down when the distance between the source and station is short, so we compute kernels using NACT for epicentral distances larger than  $15^\circ$ , and PAVA for shorter distances. Neither PAVA nor NACT consider off-great circle plane sensitivity (i.e. focusing effects, e.g. [Zhou et al. \(2005\)](#)). These effects become important for accurate amplitude fitting. With our choice of misfit function, we are first and foremost fitting the phase, and for that, the 2D effects in the vertical plane are dominant, and

important especially for overtones, as illustrated in Mégnin and Romanowicz (1999), Romanowicz et al. (2008).

## 3 Results

The tomographic inversion results for  $V_S$  and  $\xi$  are presented in figures 5 and 6 respectively. We divide the model description and interpretation into two parts, focusing first on the continent-wide structure and then, in more detail, on eastern different regions. Purpose: Is there a link between age of the crust and the lithospheric structure Do images give us insight on cratonoza-tion process - to compare with known process and thermal - chemistry data Deformation of the lithosphere by hotspot basal drag

### 3.1 Continental model

En attendant le code de cluster analysisde Marco je n'ai pas touche a cette partie

As observed in many other studies, the average isotropic shear velocity  $V_S$  in the shallow upper mantle beneath North America (NA) is high compared to the global average, which contains contributions from large oceanic regions

(Figure 7). The difference persists until  $\sim 270$  km depth and then fades away, though,  $V_S$  remains slightly higher in NA than in the global average. Compared to the continental average, precambrian provinces like Wyoming, Yavapai, Mazatzal, Great Rhyolites and Grenville are characterized by slower velocities. The cordillera region shows the slowest velocities, close the global average as for  $\xi$ . Closer to the center of the continent, region like Slave, T.H.O, Juvenile arcs and orogens (e.g. Wopmay), Superior; show higher velocities with the Slave province characterized by a positive gradient above 100 km deep.

The average of  $\xi$  is higher than 1 (which means that  $V_{SH} > V_{SV}$ ), but lower than the global average, the latter influenced by the strong  $\xi > 1$  oceanic signature. Both trends are similar with depth, but the maximum in  $\xi$  is slightly deeper than in the global average and the change from  $V_{SH} > V_{SV}$  to  $V_{SH} < V_{SV}$  is reached at  $\sim 420$  km. At shallower depths than 200 to 220 km, strongest variations relative the continental average are observed ( $+/-4$ to $8\%$ , compared to  $+/-1$ to $3\%$ ). Alternations of positive and negative gradient are observed from 50 to 400 km with peak values diminishing along depth.

## 3.2 Beneath the craton

### 3.2.1 Lateral edges

Our study confirms the presence of a thick lithospheric root in the craton with faster than average  $V_S$  down to 250 km depth, with highest velocities,  $\sim 4.7 \text{ km.s}^{-1}$ , located at depths shallower than 150 km (e.g. Figure 8 and 9). Laterally, the cratonic root in  $V_S$  coincides roughly with precambrian aged crust (see Figure 5 from 60 to 150 km deep and Figure 8.a ). The western edge of the craton follows the RMF (black thick dashed line in Figure 5), instead of the western breakup line (See the red dashed line in Figure 5 which coincides with RMF in Canada, but is diverging westward in the U.S.). While the eastern/south-eastern coincides with the Llano-Grenville Front (See the blue thin line in Figure 5) instead of the 650 Ma easter rift margin as observed in Yuan and Simons (2014) and Schaeffer and Lebedev (2014). However at 60 km, fast velocities are in better agreement with the 650 Ma easter rift margin. The northern part ends at the coastline of the Arctic ocean including the arctic archipelago and Greenland.

### 3.2.2 age of the crust and its corresponding lithosphere

These lateral edges, coinciding with precambrian crust, are well observed down to 150 km depth. Below that, the lithospheric core retracts toward the center of the precambrian continent comprising north western Juvenile arcs and orogens (e.g. Wopmay and BHT), north-eastern part of Juvenile crusts (e.g Yavapai/Mazatzal/Gr. Rhyolite), Slave, Hearne/Rae and western Superior cratons; while eastern Superior and Wyoming are cast out, as shown in Figure 5. This is consistent with the global study of Bozdağ et al. (2016) but in contrast with recent regional (e.g. Yuan et al. 2014; 2011, Schaeffer and Lebedev 2014, Nettles and Dziewoński 2008) and global (e.g French and Romanowicz 2014, French et al. 2011) studies, where the core is located at the north-east part of the continent.

There are no obvious correlations between the age of a province with amplitude of anomalies and their extension in depth. Such observation is in agreement with several studies ( (e.g for Baltic shield study Bruneton et al. 2004), (for Australian shield Fishwick et al. 2005),(e.g for north American shield study Villemaire et al. 2012, Darbyshire et al. 2013, Porritt et al. 2015) ).

For example, in 5, archaean eastern Superior craton has  $\sim 0\% V_S$  anom-

lies below 200 km (compared to  $\sim + 4\% V_S$  beneath the western Superior), similar to the proterozoic Grenville province as observed by [Villemaire et al. \(2012\)](#), [Bozdağ et al. \(2016\)](#) and archaean Wyoming ( also observed in Gao et al. 2002, Griffin et al. 1998, Menzies et al. 1993, Menzies et al. 2007); while the proterozoic belt of THO at its western part, shows as high anomalies at the same depth as within the archaean Slave or western Superior lithosphere.

Everywhere within the lithospheric core, from 60 to 100-150 km  $V_S$  increases with depth (positive velocity gradient with depth) with a maximum of  $\sim 4.7\text{-}4.8 \text{ km.s}^{-1}$  between 100 and 150 km (See Figure 9 and 8). Deeper, a negative gradient of  $V_S$  is observed, marking the base of the lithospheric core ([Eaton et al. 2009](#)), with a minimum of  $\sim 4.6 \text{ km.s}^{-1}$  that can be reached down  $\sim 270$  km deep. We identify the cratonic root by the contour of  $V_S = 4.68 \text{ km.s}^{-1}$  in Figure 8, which is chosen for clarity in order to show how variable the depth of the cratonic root is observed in our model. The  $V_S = 4.68 \text{ km.s}^{-1}$  dashed line corresponds roughly to the middle of a zone of decreasing  $V_S$  (negative velocity gradient with depth) which reaches a minimum almost uniformly around 250-270 km depth, although there are lateral variations in the strength of the minimum.

**Superior craton** The deepest roots are found in the Western and south-western Superior craton where velocities in excess of  $4.8 \text{ km.s}^{-1}$  are found at depths between 250 and 270 km (e.g. fig 8 profiles BB' and EE'). In contrast, the eastern Superior craton lithosphere is much thinner, around 150 km, with fastest velocities correspondingly peaking at depths less than 100 km as shown in fig 8 profiles BB' and FF'. Such observations show that, the link between the age of the crust and the thickness of the lithospheric upper mantle beneath, is not straightforward.

**Slave craton** In the north, the Slave cratonic lithosphere is  $\sim 250$  km thick (see Fig 8, cross sections AA' and DD'), but does not show as fast velocities as within the southwestern/western superior craton. With shear velocities in the depth range 100-150 km not exceeding  $4.7 \text{ km.s}^{-1}$ . A value slower than in Chen et al. (2007). I only have studies from RF so far(Snyder etc...), I am digging for more recent papers...

**THO** At the western part (Canadian part only) of the THO, the lithosphere is 250 km thick (see fig 8 profiles AA' and FF' and profile CC' in fig. 9), while a 100 km thinning is observed at the eastern part (i.e beneath the Hudson bay)

It is interesting to notice that at shallower depths than 100 km, the western part of the THO which welded the Superior and Rae/Hearne cratons (Hoffman 1988), shows lighter (i.e, +4% compared to +8%) positive anomalies than its archaean surrounding. The western part of the THO comprises the archaean aged Sask craton (See Figure 1). The mantle beneath this exotic craton is interpreted to have been detached and replaced by both the Superior and the Hearne mantle lithosphere during final collision of the orogen (Németh et al. 2005). This interpretation, according to Faure et al. (2011) can be extrapolated farther to the east and may explain why Trans-Hudson orogen has no imprint in the upper mantle. However, the Hudson bay's local study from Derbyshire et al. (2013) , showed that the THO shows a channel of slow velocities compare to its surrounding down to 180 km deep.

**Yavapai/Mazatzal/Granit-Rhyolite orogens** The southernmost extension of the craton (Yavapai/Mazatzal/Granit-Rhyolite orogens) represent zones of accretion for Proterozoic material and mark the amalgamation of the archean cores (Hoffman 1988). It shows a weaker but deep root (cross sections EE' and CC' in fig. 8 and map at 250 km depth in fig. 5) with velocities of almost  $4.7 \text{ km.s}^{-1}$ . There is some indication of incursion from

rifting (section EE') separating these younger crustal regions from the Superior craton. It is interesting to note that, beneath Nebraska and Kansas, the high velocity anomaly is located where cretaceous aged kimberlites are sampled. These kimberlites indicate a lithosphere thickness of about 160 km and have been affected by asthenospheric upwelling related to the Mid-Continent Rift System. (Griffin et al. 2004)

The minimum in velocity is present everywhere at a roughly constant depth beneath the cratons while the base of this low velocity zone (LVZ) is found everywhere, including outside of the cratons between 300 and 325 km depth. That base is very smooth, compared to the structures above, and its minor undulations mirror the thickness of the lithosphere above, with slight upwarping beneath the deepest cratons. The LVZ is very thin and velocity reductions are small (min.  $4.65 \text{ km.s}^{-1}$ ) beneath regions where the lithosphere is thicker than 200 km, but thicker and more pronounced under the eastern superior (min.  $4.58 \text{ km.s}^{-1}$ ). In the regions bordering the cratons, i.e. outside of RMF and Grenville Front, the low velocity minimum is between 100-150 km and very pronounced ( $V_S \approx 4.4 \text{ km.s}^{-1}$ ), and the transition out of it is more gradual, extending over 150 km depth to reach velocities of  $4.7 \text{ km.s}^{-1}$ .

### 3.2.3 Radial anisotropy structure

As observed in Babuška et al. (1998), Gung et al. (2003), Yuan et al. (2014), there are large lateral negative variations  $\xi$  down to  $\sim 200\text{km}$  depth, with regions of reduced radial anisotropy, in contrast to the more uniform, positive  $dln(\xi)$  structure in this depth range in the oceans (See figure 6 where  $dln(\xi)$  are shown according the Isotropic case ( $\xi = 1$ )).

Below 250km, it is interesting to note that there is a large band of positive  $dln(\xi)$  crossing the whole continent (across the US), making the connection between the Pacific and Atlantic mantles. This feature is not present in most of Canada, where negative  $dln(\xi)$  structure persist down to 400km and can be linked with the deep strong  $\xi$  layer of Gung et al. (2003). Our higher resolution model shows that this layer of strong  $\xi$  may not be present beneath the whole cratonic lithosphere and it seems that this feature is marking a connection with Low Velocity Fingers (LVF) observed by French et al. (2013). Generally,  $\xi$  always appears higher than 1. Except between 60 and 100 km, lower than 1 of  $\xi$  ( $V_{SV} > V_{SH}$ ) are observed in Mexico, at the southern part of Florida, the southern part of the Superior craton comprising the Mid Continental rifting, the southern part of the Granit Rhyolite Province comprising the Failed Rifting area, a large area comprising southern Hearne,

Medicine hat, northern Wyoming, B.H.T, Cordillera; and finally beneath Baffin Island.

Still need to do talk about the periodi upward of xi from depth to link with 10

To summarize, as observed in many previous tomographic studies of North America, we observe a lithospheric core beneath the Precambrian shield characterized by high  $V_S$  and reduced  $\xi$ . According to our higher resolution model, we dont observe a direct link between the age of the crust and its underlying lithosphere. Most of the core is located beneath precambrian crust but the history of the amalgamation and destruction (e.g convective removal, see Lee et al. (2011)) of the craton complexified the structure of its lithosphere. This is the case for the archean Wyoming craton who does not share the same characteristic as other Archaean blocks (e.g Slave, Hearne, Rae, western Superior) and may have suffered from basal erosion (King 2005, Lee et al. 2011). Moreover, we observe that the eastern lithospheric block of the archean Superior craton, also doesn't share the cratonic lithospheric structure. In the next chapter we will focus on this craton that may have endured basal deformation, or weakening, induced by the passage of the Great Meteor chain of hotspot.

### 3.3 Basal traction beneath the lithosphere

Ici faire le lien avec les circle figure, fingers de Scott. Probleme pratique: La carte geol ne va pas jusquau MAR et donc afficher le track n'ira pas jusqau bout... Avec la figure 11

As in Schaeffer and Lebedev (2014), Yuan et al. (2014), James et al. (2014), Silveira and Stutzmann (2002), Mocquet and Romanowicz (1990), we observe along the negative anomaly structure following the Appalachian continental shelf, a stretched positive anomaly structure from the Suwanne terrane in Florida to the Avalonian terranes of New-Scotland. At 60 km, it is made of several blocks of at most +3% anomalies embedded in a +2% structure, associated with zero to positive  $\xi$  anomalies. Below 100 km the pan african lithosphere (Yuan et al. 2014) is cut in two by a slow velocity anomaly comprising both the Great Meteor Track (GMT) and Bermuda tracks, and further southeast, the Low Velocities Fingers (LVF) observed in French et al. (2013). This is best observed in figure 11. Further East, the slow anomaly follows the GMT crossing the continental shelf, Appalachian and Grenville orogens down to 200 km. This slow anomaly corresponds to the V-shape dent, or divot, observed by van der Lee and Nolet (1997) who explained the feature by the presence of water in the mantle. We observe at 250 km that the

slow anomaly go further inland and crosses the Superior Craton northward until the Hudson bay following the GMT.

Our model images a slow velocity anomaly in agreement with the reconstruction of the Great Meteor Track proposed by Heaman and Kjarsgaard (2000). In figure 9 the cross-section DD' follows the Great Meteor track and shows the thinning of the cratonic lithosphere that may be attributed to the passage of the Great Meteor hotspot during the opening of the atlantic ocean. It is interesting to note that the low velocity channel beneath the base of the lithosphere shows lower velocities than usually observed beneath the other Archaean cratons.

After accretion of the Appalachian terranes to eastern Laurentia during the Paleozoic, no further significant episodes of magmatism or tectonism affected the western Superior region until the passage of the Great Meteor hotspot at 200110 Ma Heaman and Kjarsgaard (2000), Villemaire et al. (2012). Xenoliths analysis from kimberlites at Kirkland Lake (south eastern part of the western Superior) exhibit some evidence of diamonds, i.e, the base of the lithosphere was deeper than 170 km at the time of kimberlitic eruption (Jones et al. 2014) estimated at 160 – 152 Ma by Heaman and Kjarsgaard (2000), Heaman et al. (2003). This can be interpreted as either the litho-

sphere is today thick, and the lower lithosphere was not sampled by xenolith entrainment in the kimberlitic magmas (but nevertheless diamonds were entrained); or the lowermost lithosphere has been eroded away since eruption, possibly by the movement of the North American plate over the Great Meteor hotspot (Heaman and Kjarsgaard 2000, Villemaire et al. 2012, Jones et al. 2014). In the study of Faure et al. (2011), 23 % of kimberlite samples from southern Superior region contain diamonds. In contrast with 78 % at the northern Superior. This means that the diamond stability field within the mantle has been deteriorated through time and kimberlites that have passed across the mantle during/after such deterioration have less chances to intercept diamonds. (Faure et al. 2011)

Davies (1994) described a process of thermo-mechanical erosion which involves heating-softening of the lithospheric base by a plume tail, followed by mechanical removal of the material due to convective transfer. (Rondenay et al. 2000) Kaban et al. (2015) proposed that basal drag induced by plate motion caused a south-western shift of the Superior's cratonic root. A feature that was observed by the local inversion of gravity, topography, crustal structure and seismic data. This basal deformation would have been enabled by the reheating of the lithosphere due to the passage of the Great Meteor

hotspot (see Eaton and Frederiksen 2007, Kaban et al. 2015).

Our observations show that despite the archaean age of the Superior craton, the lithospheric root thickness of a craton is not flat and can be altered as broadly observed within the eastern part of the Superior craton.

Notes for interprating Xenoliths studies. SEE DATATION OF GMT Model

## 4 Figure

## References

Abt, D. L., Fischer, K. M., French, S. W., Ford, H. A., Yuan, H., and Romanowicz, B. (2010). North american lithospheric discontinuity structure imaged by PsandSpreceiver functions. *Journal of Geophysical Research*, 115(B9).

Babuška, V., Montagner, J.-P., Plomerová, J., and Girardin, N. (1998). Age-dependent large-scale fabric of the mantle lithosphere as derived from surface-wave velocity anisotropy. In *Geodynamics of Lithosphere & Earths Mantle*, pages 257–280. Springer.

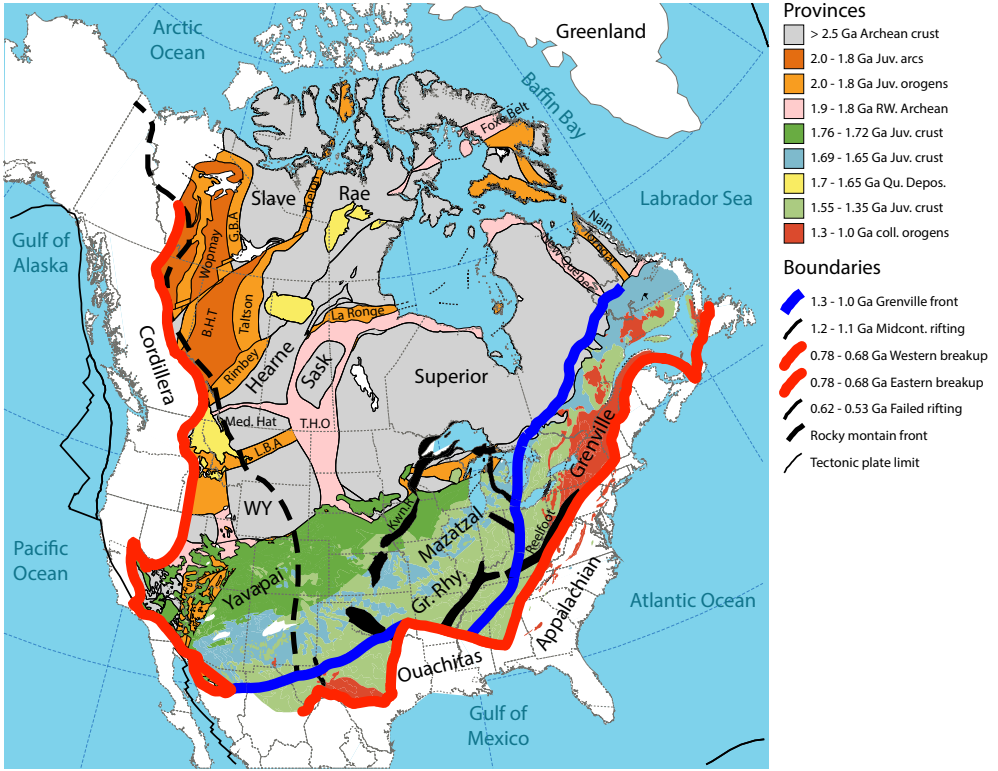


Figure 1: Large scale Precambrian architecture of North America (modified from Whitmeyer and Karlstrom (2007)). Colours indicate ages of different regions, as shown in the legend. The stable cratonic core is defined by the Rocky Mountain Front to the west (dashed dark grey line), defined by the surface trace of deformation), and the appalachian front to the east (solid light red line). The solid blue line demarcates the westward extent of the Grenville/Llano Front. The solid red line along the Cordillera province demarcates the breakup of Rodinia. Solid green lines indicate tectonic plate boundaries. Abbreviations are as follows: RW, re-worked; GBA, Great Bear Arc; BHT, Buffalo Head Terrane; Taltson, Talston Arc; Rimbey, Rimbey Arc; Tornagat, Torngat Arc; L.B.A, Little Belt Arc; LRA; THO, Trans-Hudson Orogen; RGR, Rio Grande Rift; Reelfoot, Reelfoor Rift; Kwn.R, Kewanowan Rift; Sask, Sask Craton; WY, Wyoming Province; Med. Hat., Medicine Hat Block; Grt. Rhy, GraniteRhyolite Province; Grenville, Grenville Province.

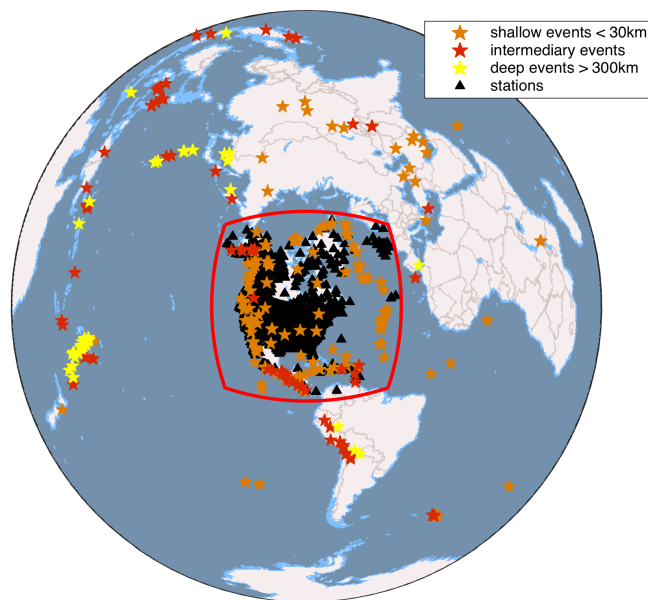


Figure 2: Source and station distribution for the new North American inversion. Black triangles show the seismic stations. Stars are 155 regional events, in addition to 122 teleseismic events. Orange stars indicate events shallower than 30 km deep, yellow stars for deeper than 300 km and red one are in between. Thick red line indicates the boundaries used for the RegSEM forward simulation, which extends 89 by 89 horizontally and down to 1600 km and contains all stations and regional events.

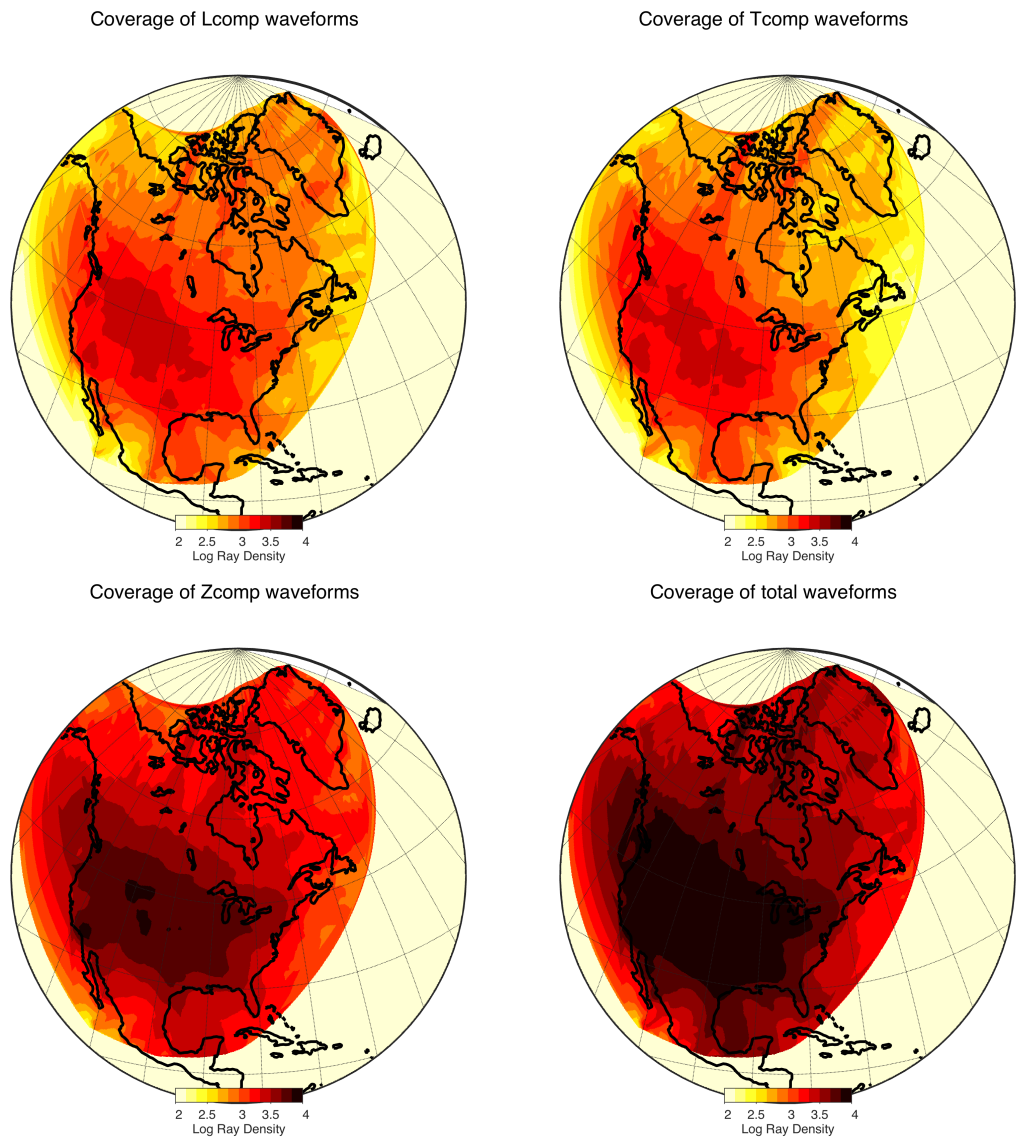


Figure 3: Density coverage for each component and all gathered.

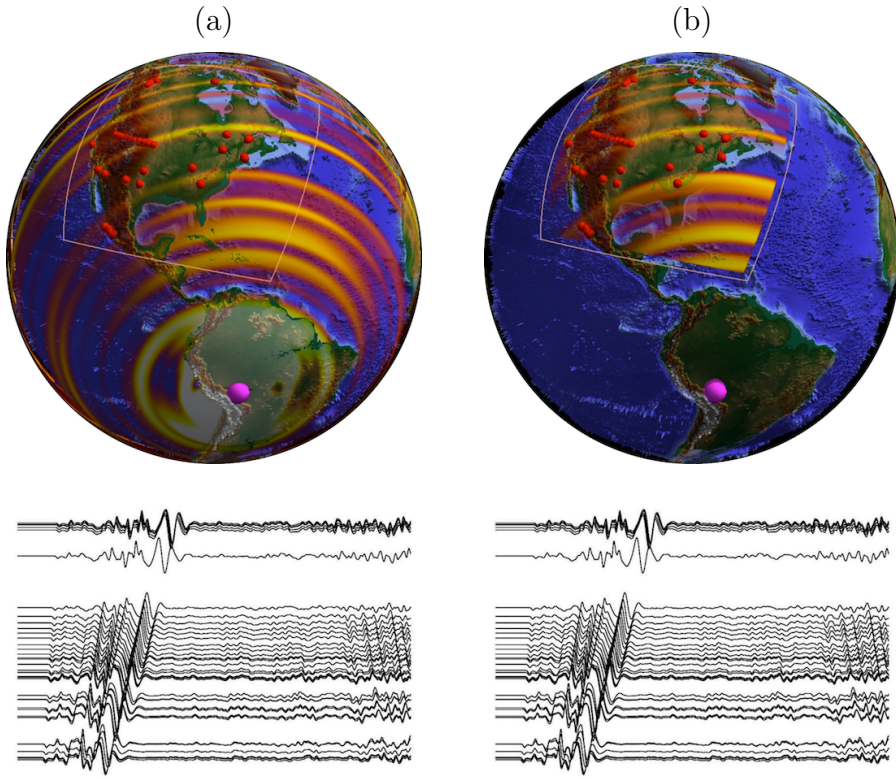
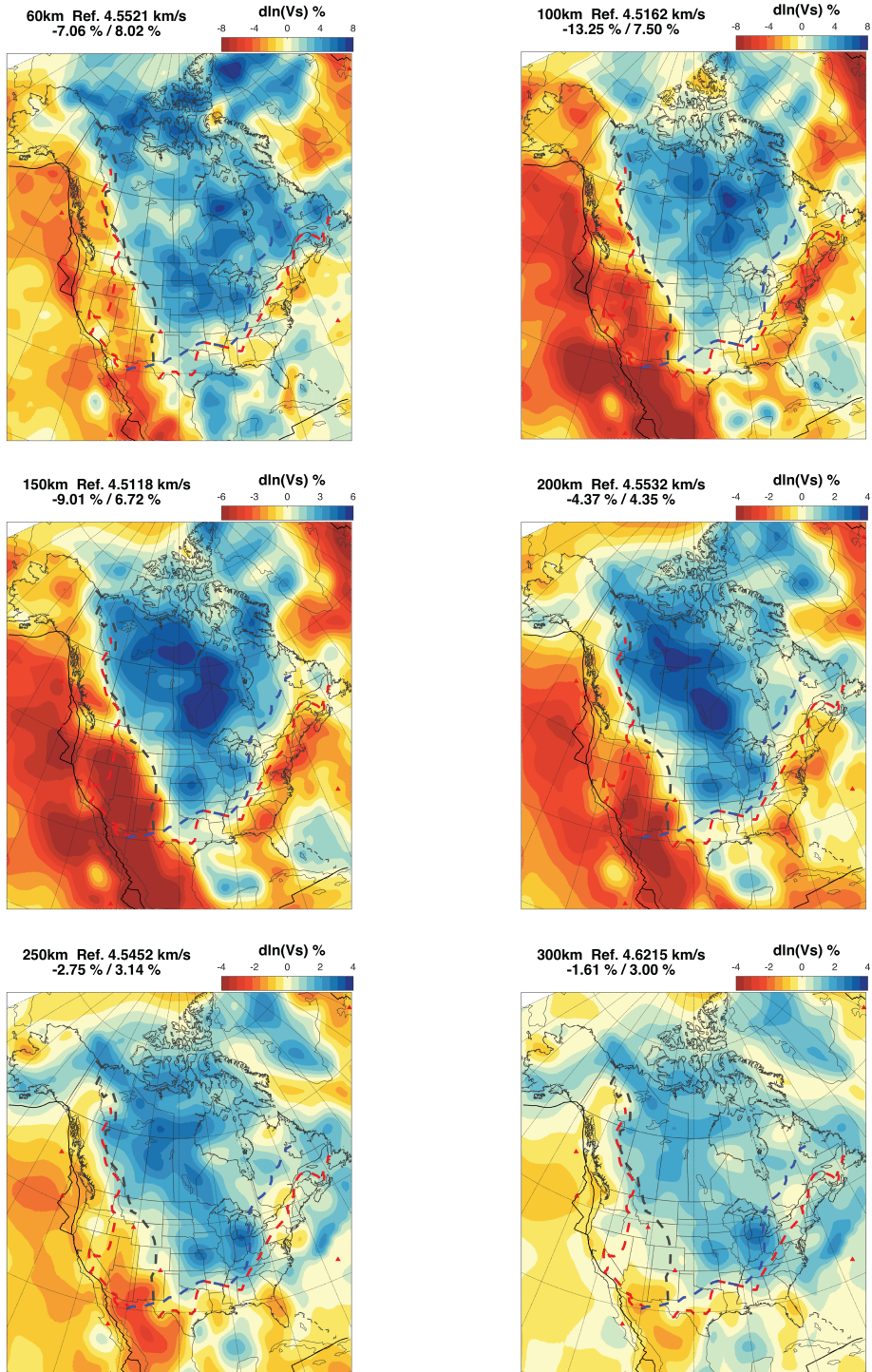
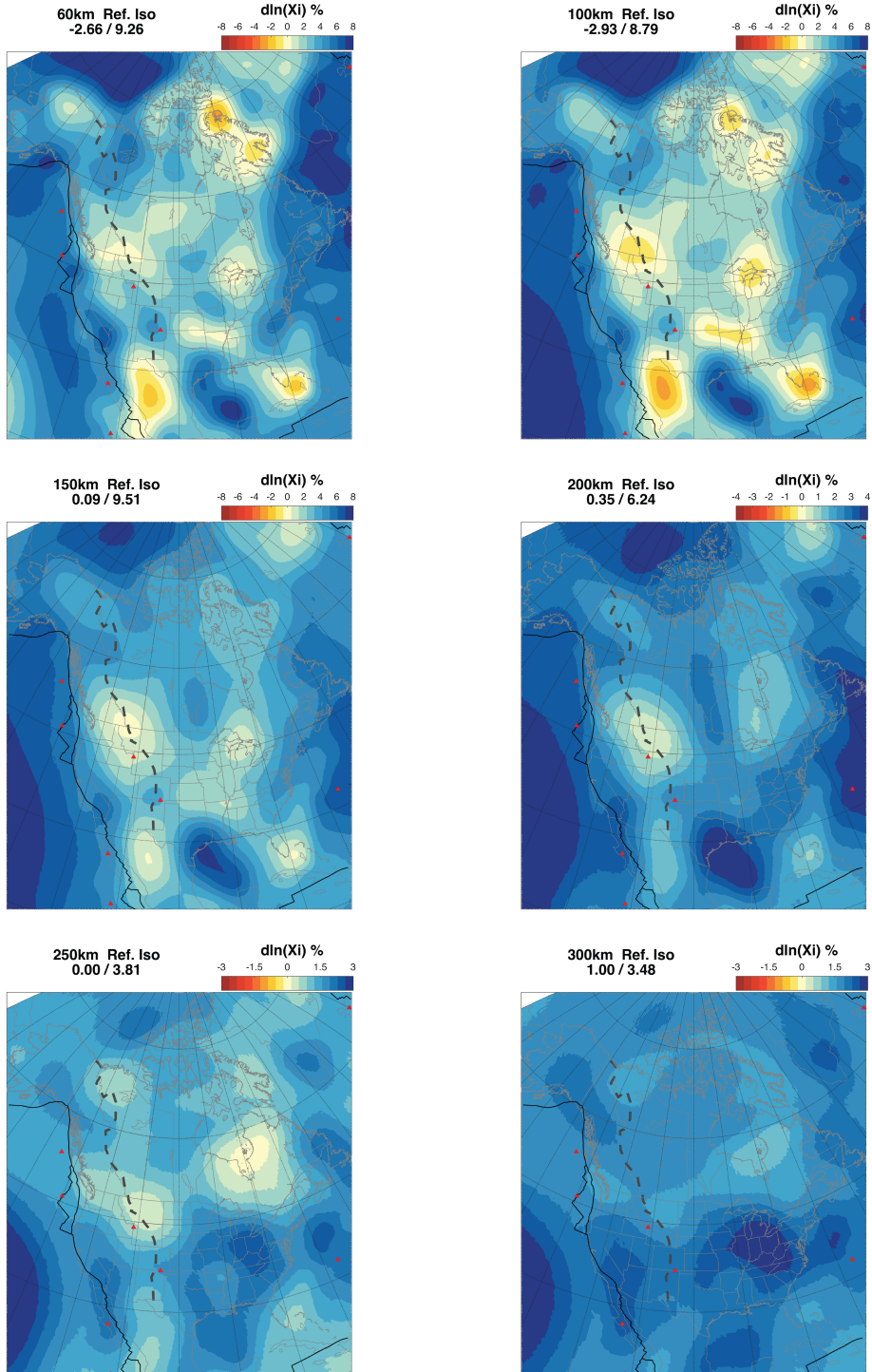


Figure 4: Comparison between a global scale simulation and a regional scale simulation of wave propagation following an earthquake in south America. The seismograms corresponds to the recordings at 37 station located in north America (red spheres). The pink sphere shows the epicenter of the earthquake. In (a), the wavefield is modeled globally using the spectral element method Specfem3D\_globe ([Komatitsch 2002](#)). In (b), the wavefield is modeled regionally using the RegSEM. During the inversion, all the synthetic seismograms are computed using the regional SEM code RegSEM ([Cupillard et al. 2012](#)) code and regenerated thanks to virtual sources located around the computational domain (see [Masson et al. 2013](#)). The sismograms in (b) are exactly similar to those in (a), however, the computational effort is greatly reduced in the regional simulation (b).



39  
 Figure 5: 3D isotropic shear wave velocity structure of the continent. Map views are shown from 60 km down to 300 km, as variations with respect to the regional mean (thick red line in Figure 7) as  $\frac{dV_S}{V_{S_O}}$ . Below each map, depth and its regional shear velocity mean is indicated. Minimum and maximum perturbations are also indicated.



40  
 Figure 6: 3D radial anisotropic structure of the continent. Map views are shown from 60 km down to 300 km, as variations with respect to the regional mean (thick red line in Figure 7) as  $\frac{d\xi}{\xi_0}$ . Below each map, depth and its regional shear velocity mean is indicated. Minimum and maximum perturbations are also indicated.

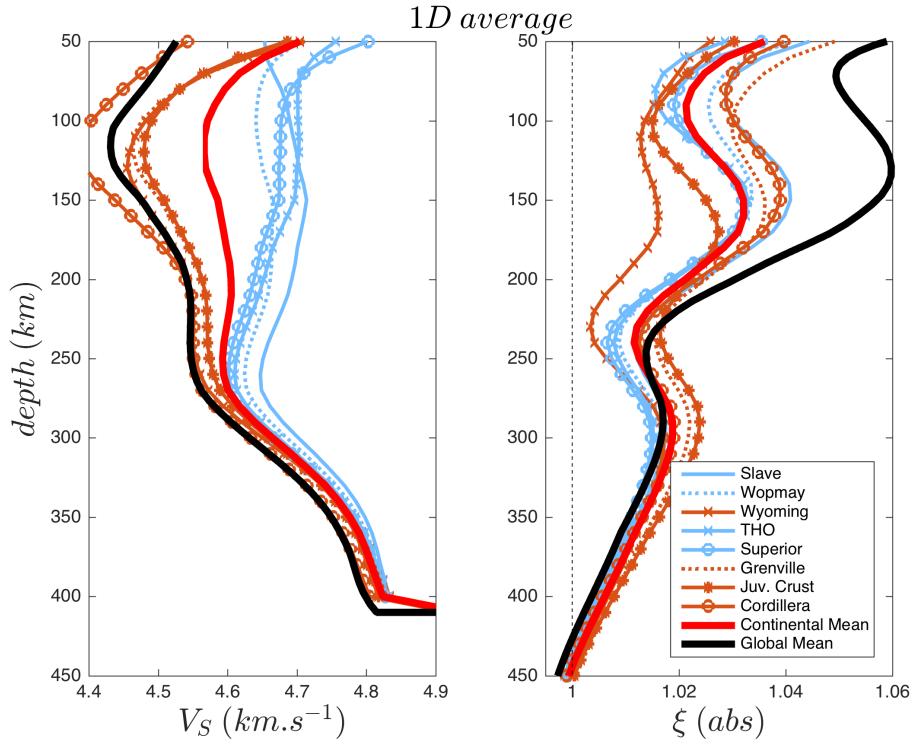


Figure 7: 1D average depth profiles for isotropic shear velocity (left) and radial anisotropy (right), for the SEMucb\_wm1 global model (thick black), the continental average (thick red); and depth profiles for different regions in the model (see legend and Figure 1). The continental average is always higher than the global average in terms of  $V_S$ , while for  $\xi$ , they are similar deeper than 250 km.

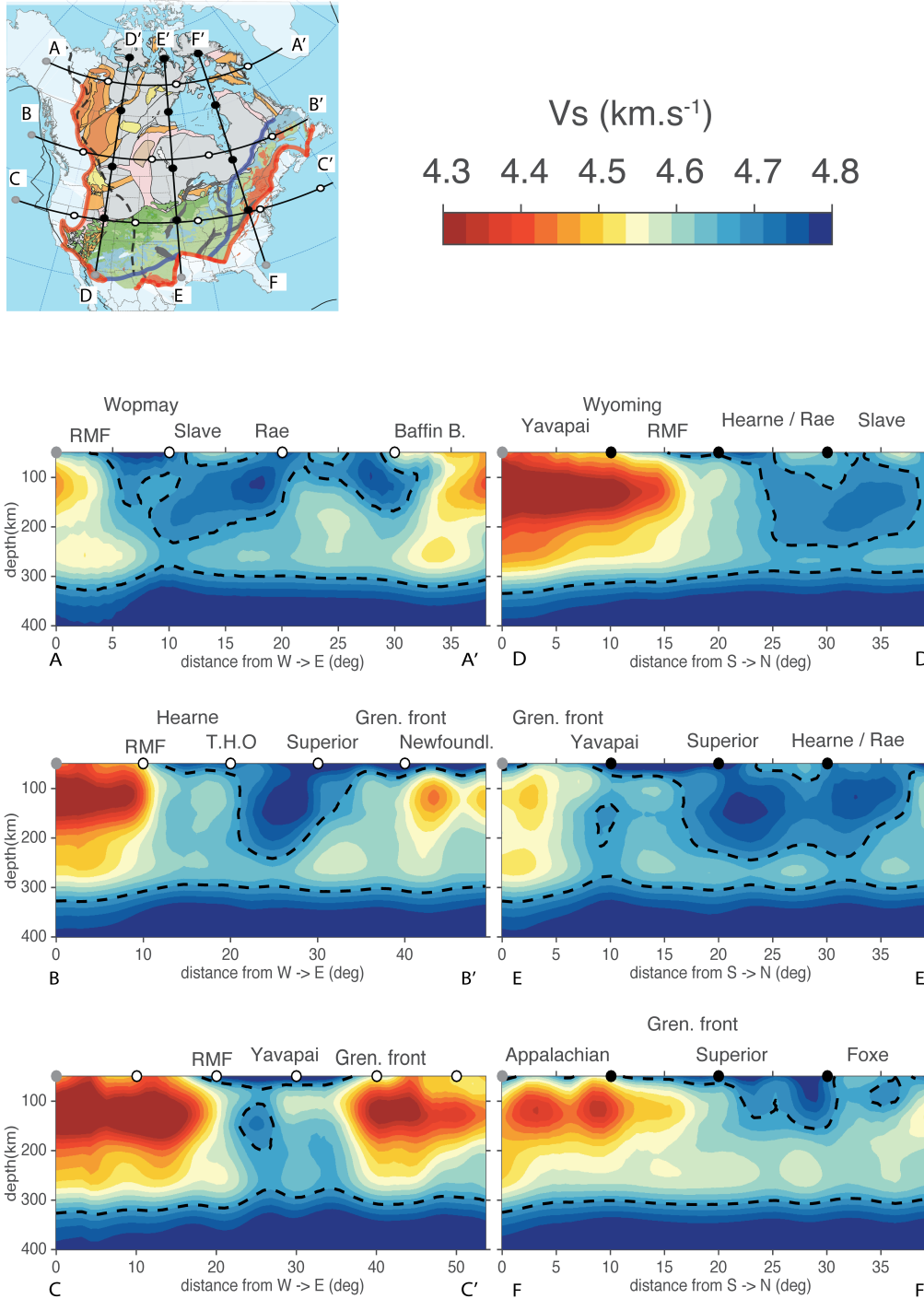


Figure 8: Cross Section of the lithospheric core at its edges. Cross Section of the lithospheric core with absolute velocities of  $V_S$  in km.s $^{-1}$ .

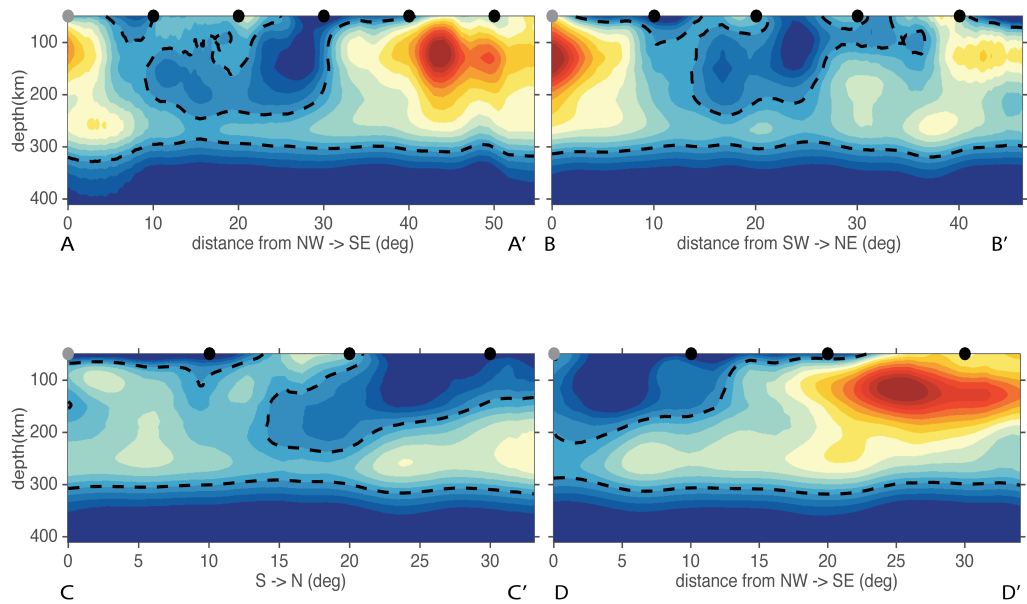
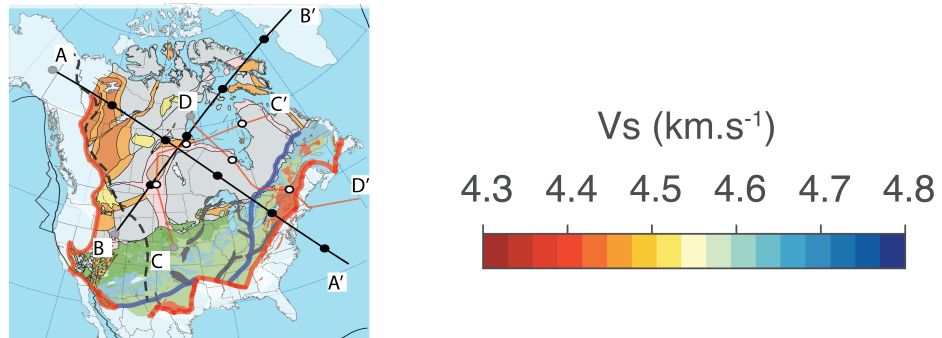


Figure 9: Cross Section of the lithospheric core. Cross Section of the lithospheric core with absolute velocities of  $V_S$  in km.s<sup>-1</sup>.

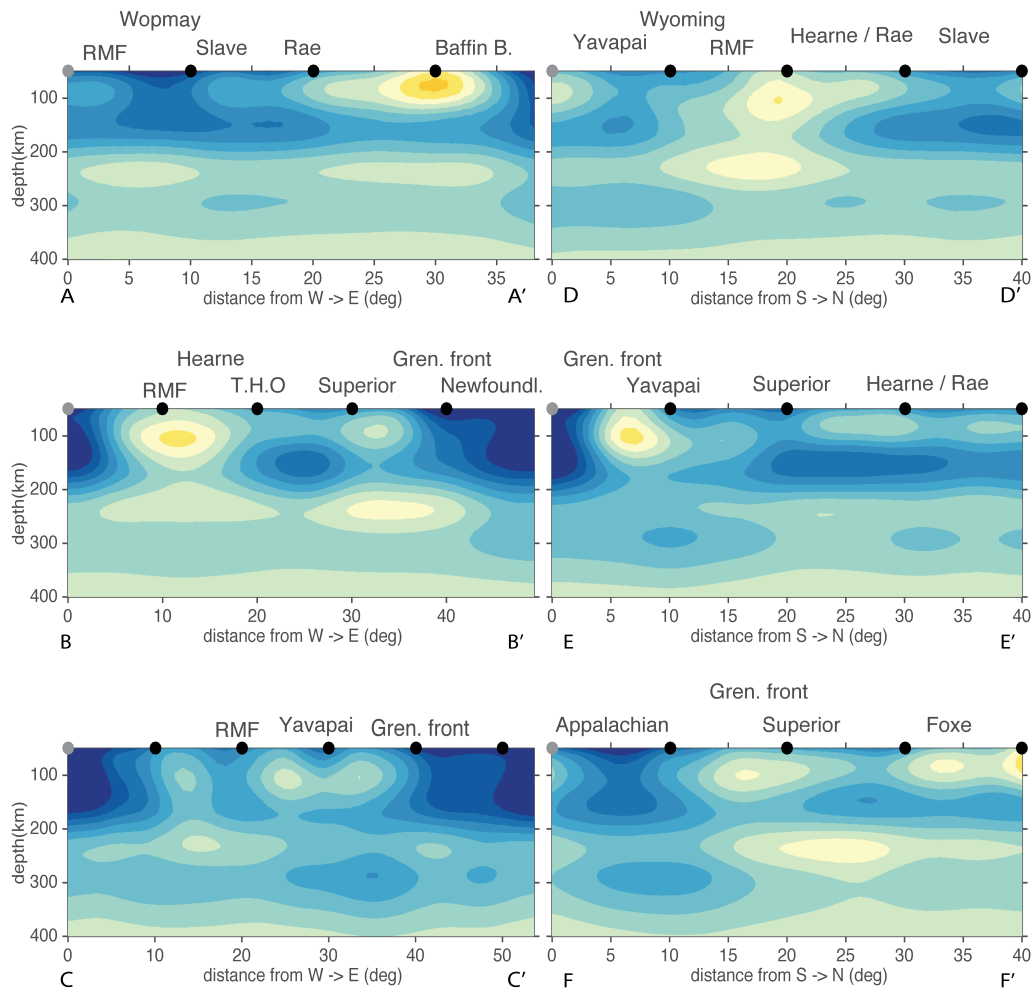
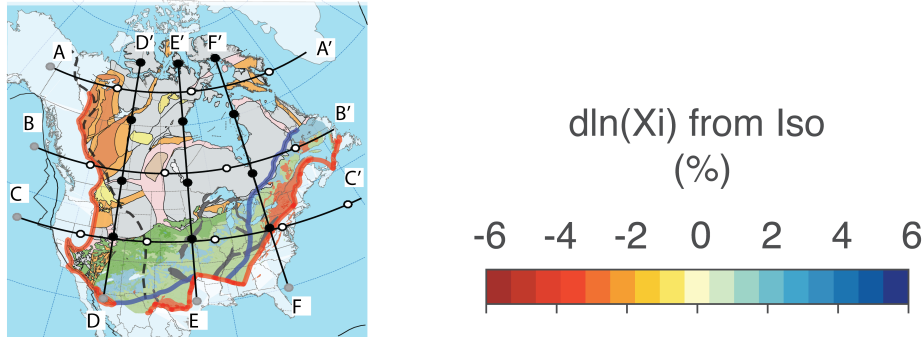


Figure 10: Cross Section of the lithospheric core at its edges. Cross Section of the lithospheric core with perturbations of  $\xi$  in % with respect to the isotropic case (i.e  $\xi = 1$ ).

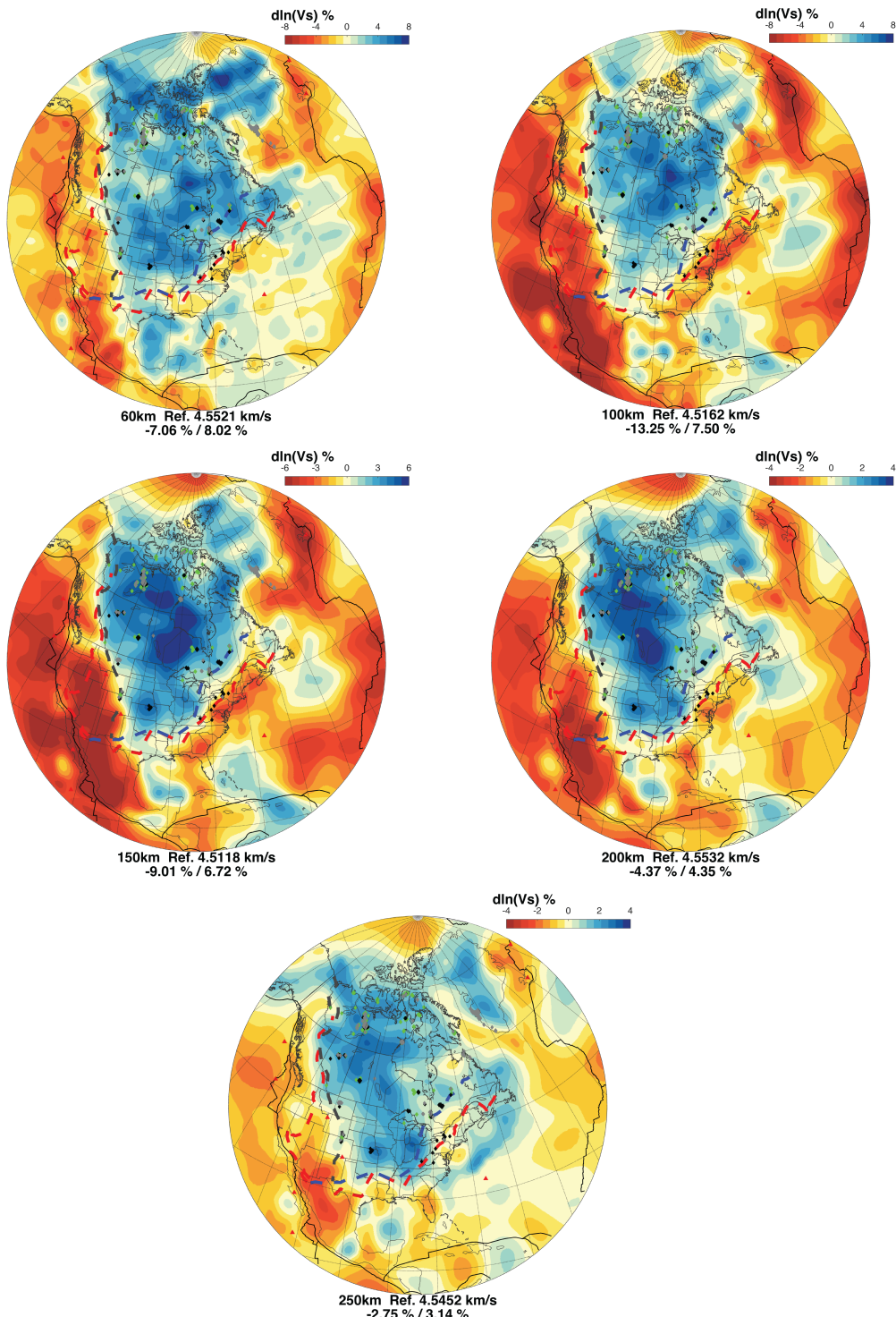


Figure 11: 3D isotropic shear wave velocity structure of the continent embedded in SEM\_ucbwm1 (starting model). Map views are shown from 60 km down to 250 km, as variations with respect to the regional mean as  $\frac{dV_S}{V_{S_O}}$ . Below each map, depth and its regional shear velocity mean is indicated. Minimum and maximum perturbations are also indicated..

- Backus, G. E. (1962). Long-wave elastic anisotropy produced by horizontal layering. *Journal of Geophysical Research*, 67(11):4427–4440.
- Bassin, C., Laske, G., and Masters, G. (2000). The current limits of resolution for surface wave tomography in north america. *EOS Trans AGU*.
- Bedle, H. and van der Lee, S. (2009). Svelocity variations beneath North America. *Journal of Geophysical Research*, 114(B7).
- Bostock, M. (1998). Mantle stratigraphy and evolution of the slave province. *Journal of Geophysical Research: Solid Earth*, 103(B9):21183–21200.
- Bozdağ, E., Peter, D., Lefebvre, M., Komatitsch, D., Tromp, J., Hill, J., Podhorszki, N., and Pugmire, D. (2016). Global adjoint tomography: First-generation model. *Geophysical Journal International*, page ggw356.
- Bruneton, M., Pedersen, H. A., Farra, V., Arndt, N. T., Vacher, P., Achauer, U., Alinaghi, A., Ansorge, J., Bock, G., Friederich, W., et al. (2004). Complex lithospheric structure under the central baltic shield from surface wave tomography. *Journal of Geophysical Research: Solid Earth*, 109(B10).
- Burdick, S., Van der Hilst, R. D., Vernon, F. L., Martynov, V., Cox, T., Eakins, J., Karasu, G. H., Tylell, J., Astiz, L., and Pavlis, G. L.

- (2014). Model update january 2013: Upper mantle heterogeneity beneath north america from travel-time tomography with global and usarray transportable array data. *Seismological Research Letters*, 85(1):77–81.
- Calò, M., Bodin, T., and Romanowicz, B. (2016). Layered structure in the upper mantle across North America from joint inversion of long and short period seismic data. *Earth and Planetary Science Letters*, 449:164–175.
- Capdeville, Y. and Marigo, J.-J. (2008). Shallow layer correction for spectral element like methods. *Geophysical Journal International*, 172(3):1135–1150.
- Chen, C.-W., Rondenay, S., Weeraratne, D. S., and Snyder, D. B. (2007). New constraints on the upper mantle structure of the slave craton from rayleigh wave inversion. *Geophysical Research Letters*, 34(10).
- Cleary, J. and Hales, A. L. (1966). An analysis of the travel times of p waves to north american stations, in the distance range 32 to 100. *Bulletin of the Seismological Society of America*, 56(2):467–489.
- Cupillard, P., Delavaud, E., Burgos, G., Festa, G., Vilotte, J.-P., Capdeville, Y., and Montagner, J.-P. (2012). RegSEM: a versatile code based on

the spectral element method to compute seismic wave propagation at the regional scale. *Geophysical Journal International*, 188(3):1203–1220.

Darbyshire, F. A., Eaton, D. W., and Bastow, I. D. (2013). Seismic imaging of the lithosphere beneath hudson bay: Episodic growth of the laurentian mantle keel. *Earth and Planetary Science Letters*, 373:179–193.

Davies, G. F. (1994). Thermomechanical erosion of the lithosphere by mantle plumes. *Journal of Geophysical Research: Solid Earth*, 99(B8):15709–15722.

Debayle, E. and Ricard, Y. (2012). A global shear velocity model of the upper mantle from fundamental and higher Rayleigh mode measurements. *Journal of Geophysical Research: Solid Earth*, 117(B10).

Deschamps, F., Lebedev, S., Meier, T., and Trampert, J. (2008). Stratified seismic anisotropy reveals past and present deformation beneath the east-central United States. *Earth and Planetary Science Letters*, 274(3-4):489–498.

Eaton, D. W., Darbyshire, F., Evans, R. L., Grtter, H., Jones, A. G., and Yuan, X. (2009). The elusive lithosphere–asthenosphere boundary (LAB) beneath cratons. *Lithos*, 109(1-2):1–22.

- Eaton, D. W. and Frederiksen, A. (2007). Seismic evidence for convection-driven motion of the north american plate. *Nature*, 446(7134):428–431.
- Faure, S., Godey, S., Fallara, F., and Trépanier, S. (2011). Seismic architecture of the archean north american mantle and its relationship to diamondiferous kimberlite fields. *Economic Geology*, 106(2):223–240.
- Fischer, K. M., Ford, H. A., Abt, D. L., and Rychert, C. A. (2010). The lithosphere-asthenosphere boundary. *Annu. Rev. Earth Planet. Sci.*, 38(1):551–575.
- Fishwick, S., Kennett, B., and Reading, A. (2005). Contrasts in lithospheric structure within the australian cratoninsights from surface wave tomography. *Earth and Planetary Science Letters*, 231(3):163–176.
- Ford, H. A., Long, M. D., and Wirth, E. A. (2016). Midlithospheric discontinuities and complex anisotropic layering in the mantle lithosphere beneath the wyoming and superior provinces. *Journal of Geophysical Research: Solid Earth*, 121(9):6675–6697.
- French, S., Lekic, V., and Romanowicz, B. (2011). Global waveform tomography with the spectral element method: A second-generation upper-mantle model. *Geophys. J. Int*, 170(2):823–838.

French, S., Lekic, V., and Romanowicz, B. (2013). Waveform tomography reveals channeled flow at the base of the oceanic asthenosphere. *Science*, 342(6155):227–230.

French, S. W. and Romanowicz, B. A. (2014). Whole-mantle radially anisotropic shear velocity structure from spectral-element waveform tomography. *Geophysical Journal International*, 199(3):1303–1327.

Grand, S. P. and Helmberger, D. V. (1984). Upper mantle shear structure of North America. *Geophysical Journal International*, 76(2):399–438.

Griffin, W., O'Reilly, S. Y., Doyle, B., Pearson, N., Coopersmith, H., Kivi, K., Malkovets, V., and Pokhilenko, N. (2004). Lithosphere mapping beneath the north american plate. *Lithos*, 77(1):873–922.

Gung, Y., Panning, M., and Romanowicz, B. (2003). Global anisotropy and the thickness of continents. *Nature*, 422(6933):707–711.

Heaman, L. and Kjarsgaard, B. (2000). Timing of eastern north american kimberlite magmatism: continental extension of the great meteor hotspot track? *Earth and Planetary Science Letters*, 178(3):253–268.

Heaman, L., Kjarsgaard, B., and Creaser, R. (2003). The timing of kimberlite

magmatism in north america: implications for global kimberlite genesis and diamond exploration. *Lithos*, 71(2):153–184.

Herrin, E. and Taggart, J. (1968). Regional variations in p travel times. *Bulletin of the Seismological Society of America*, 58(4):1325–1337.

Hoffman, P. F. (1988). United plates of America, the birth of a craton: Early proterozoic assembly and growth of laurentia. *Annu. Rev. Earth Planet. Sci.*, 16(1):543–603.

James, E. K., Dalton, C. A., and Gaherty, J. B. (2014). Rayleigh wave phase velocities in the atlantic upper mantle. *Geochemistry, Geophysics, Geosystems*, 15(11):4305–4324.

Jones, A. G., Ledo, J., Ferguson, I. J., Craven, J. A., Unsworth, M. J., Chouteau, M., and Spratt, J. E. (2014). The electrical resistivity of canadas lithosphere and correlation with other parameters: contributions from lithoprobe and other programmes 1. *Canadian Journal of Earth Sciences*, 51(6):573–617.

Kaban, M. K., Mooney, W. D., and Petrunin, A. G. (2015). Cratonic root beneath North America shifted by basal drag from the convecting mantle. *Nature Geoscience*, 8(10):797–800.

King (2005). Archean cratons and mantle dynamics. *Earth and Planetary Science Letters*, 234(1-2):1–14.

Komatitsch, D. (2002). The spectral-element method, beowulf computing, and global seismology. *Science*, 298(5599):1737–1742.

Kustowski, B., Ekstrm, G., and Dziewoński, A. M. (2008). Anisotropic shear-wave velocity structure of the earth's mantle: A global model. *J. Geophys. Res.*, 113(B6).

Lee, C.-T. A., Luffi, P., and Chin, E. J. (2011). Building and destroying continental mantle. *Annu. Rev. Earth Planet. Sci.*, 39(1):59–90.

Lekić, V. and Romanowicz, B. (2011). Inferring upper-mantle structure by full waveform tomography with the spectral element method. *Geophysical Journal International*, 185(2):799–831.

Levin, V., Menke, W., and Park, J. (1999). Shear wave splitting in the appalachians and the urals- a case for multilayered anisotropy. *Journal of Geophysical Research*, 104(17):975–17.

Li, X.-D. and Romanowicz, B. (1995). Comparison of global waveform in-

versions with and without considering cross-branch modal coupling. *Geophysical Journal International*, 121(3):695–709.

Li, X.-D. and Romanowicz, B. (1996). Global mantle shear velocity model developed using nonlinear asymptotic coupling theory. *J. Geophys. Res.*, 101(B10):22245–22272.

Love, A. E. H. (2013). *A treatise on the mathematical theory of elasticity*. Cambridge university press.

Marone, F., Gung, Y., and Romanowicz, B. (2007). Three-dimensional radial anisotropic structure of the north american upper mantle from inversion of surface waveform data. *Geophysical Journal International*, 171(1):206–222.

Marone, F. and Romanowicz, B. (2007). The depth distribution of azimuthal anisotropy in the continental upper mantle. *Nature*, 447(7141):198–201.

Masson, Y., Cupillard, P., Capdeville, Y., and Romanowicz, B. (2013). On the numerical implementation of time-reversal mirrors for tomographic imaging. *Geophysical Journal International*, 196(3):1580–1599.

Masson, Y. and Romanowicz, B. (2016). Box tomography: Localised imaging of remote targets buried in an unknown medium, a step forward for

understanding key structures in the deep earth. *Geophysical Journal International*.

Masson, Y. and Romanowicz, B. (2017). Fast computation of synthetic seismograms within a medium containing remote localized perturbations: a numerical solution to the scattering problem. *Geophysical Journal International*, 208(2):674–692.

Mégnin, C. and Romanowicz, B. (1999). The effects of the theoretical formalism and data selection on mantle models derived from waveform tomography. *Geophysical Journal International*, 138(2):366–380.

Mégnin, C. and Romanowicz, B. (2000). The three-dimensional shear velocity structure of the mantle from the inversion of body, surface and higher-mode waveforms. *Geophysical Journal International*, 143(3):709–728.

Mochizuki, E. (1986). The free oscillations of an anisotropic and heterogeneous earth. *Geophysical Journal International*, 86(1):167–176.

Mocquet, A. and Romanowicz, B. (1990). Three-dimensional structure of the upper mantle beneath the atlantic ocean inferred from longperiod rayleigh waves, ii. *Inversion. J. Geophys. Res.*, 95:6787–6798.

Montagner, J.-P. and Anderson, D. L. (1989). Petrological constraints on seismic anisotropy. *Physics of the Earth and Planetary Interiors*, 54(1-2):82–105.

Németh, B., Clowes, R. M., and Hajnal, Z. (2005). Lithospheric structure of the trans-hudson orogen from seismic refraction-wide-angle reflection studies. *Canadian Journal of Earth Sciences*, 42(4):435–456.

Nettles, M. and Dziewoński, A. M. (2008). Radially anisotropic shear velocity structure of the upper mantle globally and beneath North America. *J. Geophys. Res.*, 113(B2).

Panning, M. and Romanowicz, B. (2006). A three-dimensional radially anisotropic model of shear velocity in the whole mantle. *Geophysical Journal International*, 167(1):361–379.

Porritt, R. W., Allen, R. M., and Pollitz, F. F. (2014). Seismic imaging east of the rocky mountains with usarray. *Earth and Planetary Science Letters*, 402:16–25.

Porritt, R. W., Miller, M. S., and Darbyshire, F. A. (2015). Lithospheric architecture beneath hudson bay. *Geochemistry, Geophysics, Geosystems*, 16(7):2262–2275.

Poupinet, G. (1979). On the relation between p-wave travel time residuals and the age of continental plates. *Earth and Planetary Science Letters*, 43(1):149–161.

Rader, E., Emry, E., Schmerr, N., Frost, D., Cheng, C., Menard, J., Yu, C.-Q., and Geist, D. (2015). Characterization and petrological constraints of the midlithospheric discontinuity. *Geochemistry, Geophysics, Geosystems*, 16(10):3484–3504.

Ritsema, J., Deuss, A., van Heijst, H. J., and Woodhouse, J. H. (2010). S40rts: a degree-40 shear-velocity model for the mantle from new Rayleigh wave dispersion, teleseismic traveltimes and normal-mode splitting function measurements. *Geophysical Journal International*, 184(3):1223–1236.

Romanowicz, B. (1987). Multiplet-multiplet coupling due to lateral heterogeneity: asymptotic effects on the amplitude and frequency of the earth's normal modes. *Geophysical Journal International*, 90(1):75–100.

Romanowicz, B. A. (1979). Seismic structure of the upper mantle beneath the United States by three-dimensional inversion of body wave arrival times. *Geophysical Journal International*, 57(2):479–506.

Romanowicz, B. A., Panning, M. P., Gung, Y., and Capdeville, Y. (2008).

On the computation of long period seismograms in a 3-D earth using normal mode based approximations. *Geophysical Journal International*, 175(2):520–536.

Rondenay, S., Bostock, M. G., Hearn, T. M., White, D. J., and Ellis, R. M. (2000). Lithospheric assembly and modification of the se canadian shield: Abitibi-grenville teleseismic experiment. *Journal of Geophysical Research: Solid Earth*, 105(B6):13735–13754.

Schaeffer, A. and Lebedev, S. (2014). Imaging the north american continent using waveform inversion of global and USArray data. *Earth and Planetary Science Letters*, 402:26–41.

Schaeffer, A. J. and Lebedev, S. (2013). Global shear speed structure of the upper mantle and transition zone. *Geophysical Journal International*, 194(1):417–449.

Shapiro, N. M. and Ritzwoller, M. H. (2002). Monte-Carlo inversion for a global shear-velocity model of the crust and upper mantle. *Geophysical Journal International*, 151(1):88–105.

Sigloch, K. (2011). Mantle provinces under North America from mul-

tifrequencyPwave tomography. *Geochemistry, Geophysics, Geosystems*, 12(2):n/a–n/a.

Silveira, G. and Stutzmann, E. (2002). Anisotropic tomography of the atlantic ocean. *Physics of the Earth and Planetary Interiors*, 132(4):237–248.

Su, W.-j., Woodward, R. L., and Dziewonski, A. M. (1994). Degree 12 model of shear velocity heterogeneity in the mantle. *Journal of Geophysical Research: Solid Earth*, 99(B4):6945–6980.

Tarantola, A. (2005). *Inverse problem theory and methods for model parameter estimation*. siam.

Tarantola, A. and Valette, B. (1982). Generalized nonlinear inverse problems solved using the least squares criterion. *Reviews of Geophysics*, 20(2):219–232.

Thybo, H. and Perchu, E. (1997). The seismic 8 discontinuity and partial melting in continental mantle. *Science*, 275(5306):1626–1629.

Unser, M., Aldroubi, A., and Eden, M. (1993a). B-spline signal processing. i. theory. *IEEE transactions on signal processing*, 41(2):821–833.

Unser, M., Aldroubi, A., and Eden, M. (1993b). B-spline signal processing. ii.

efficiency design and applications. *IEEE transactions on signal processing*, 41(2):834–848.

Valentine, A. P. and Trampert, J. (2016). The impact of approximations and arbitrary choices on geophysical images. *Geophysical Journal International*, 204(1):59–73.

van der Lee, S. and Frederiksen, A. (2005). Surface wave tomography applied to the north american upper mantle. In *Seismic Earth: Array Analysis of Broadband Seismograms*, pages 67–80. Wiley-Blackwell.

van der Lee, S. and Nolet, G. (1997). Upper mantleSvelocity structure of North America. *Journal of Geophysical Research: Solid Earth*, 102(B10):22815–22838.

Villemaire, M., Darbyshire, F., and Bastow, I. (2012). P-wave tomography of eastern north america: Evidence for mantle evolution from archean to phanerozoic, and modification during subsequent hot spot tectonism. *Journal of Geophysical Research: Solid Earth*, 117(B12).

Wang, Z. and Dahlen, F. A. (1995). Spherical-spline parameterization of three-dimensional earth models. *Geophysical Research Letters*, 22(22):3099–3102.

Whitmeyer, S. J. and Karlstrom, K. E. (2007). Tectonic model for the proterozoic growth of north america. *Geosphere*, 3(4):220–259.

Woodhouse, J. H. and Dziewonski, A. M. (1984). Mapping the upper mantle: Three-dimensional modeling of earth structure by inversion of seismic waveforms. *Journal of Geophysical Research: Solid Earth*, 89(B7):5953–5986.

Yuan, H., French, S., Cupillard, P., and Romanowicz, B. (2014). Lithospheric expression of geological units in central and eastern North America from full waveform tomography. *Earth and Planetary Science Letters*, 402:176–186.

Yuan, H. and Romanowicz, B. (2010). Lithospheric layering in the north american craton. *Nature*, 466(7310):1063–1068.

Yuan, H., Romanowicz, B., Fischer, K. M., and Abt, D. (2011). 3-D shear wave radially and azimuthally anisotropic velocity model of the north american upper mantle. *Geophysical Journal International*, 184(3):1237–1260.

Yuan, Y. O. and Simons, F. J. (2014). Multiscale adjoint waveform-difference tomography using wavelets. *Geophysics*, 79(3):WA79–WA95.

Zhou, Y., Dahlen, F., Nolet, G., and Laske, G. (2005). Finite-frequency effects in global surface-wave tomography. *Geophysical Journal International*, 163(3):1087–1111.

Zhu, H., Bozdağ, E., and Tromp, J. (2015). Seismic structure of the european upper mantle based on adjoint tomography. *Geophysical Journal International*, 201(1):18–52.